

PAPER • OPEN ACCESS

Experimental investigation of star grains in dual thrust solid propellant motors

To cite this article: M El-Naggar *et al* 2020 *IOP Conf. Ser.: Mater. Sci. Eng.* **973** 012001

View the [article online](#) for updates and enhancements.

You may also like

- [Mitigation of irregular burning in a small solid propellant rocket motor](#)
M Elkshen, H Belal and M A Al-Sanabawy
- [Detrended cross correlation analysis \(DCCA\) of radon, thoron, temperature and pressure time series data](#)
Javid Iqbal, Kashif Javed Lone, Lal Hussain *et al.*
- [A Numerical Simulation Study for A Dual Thrust Solid Propellant Rocket Motor Nozzle](#)
Alaa R AbdelGawad and Liang Guozhu



The Electrochemical Society
Advancing solid state & electrochemical science & technology

243rd Meeting with SOFC-XVIII

Boston, MA • May 28 – June 2, 2023

Accelerate scientific discovery!

Learn More & Register



Experimental investigation of star grains in dual thrust solid propellant motors

M El-Naggar¹, H Belal² and H M Abdalla³

¹ M.Sc. Student, Rocket Department, Military Technical College, Egypt

² Assistant Professor, Rocket Department, Military Technical College, Egypt

³ Associate Professor, Rocket Department, Military Technical College, Egypt
hbelal@mtc.edu.eg

Abstract. One of the great challenges in designing tactical solid missiles is to achieve high acceleration in the boost phase then maintaining constant speed during the sustain phase. This could be achieved by using a dual thrust solid-propellant rocket motor. Many of these tactical motors use a combination of star, tubular or finocyl grains to achieve this profile. The present study uses two tandem star grains with different design parameters and different transition geometry. Previous researches had consistently shown that the main advantage of star grain is the potential higher volumetric loading in addition to high tailorability. The pressure-time curve for the designed grains is calculated using a zero-dimensional internal ballistic module and a small-scale test motor is used to verify the calculated pressure-time curve. Different transition geometries are compared. Tapered transition is shown to give a comparable performance with the sharp transition with the advantage of higher volumetric loading.

1. Introduction

The objective of Dual-Thrust Rocket Motors (DTRMs) is to generate two levels of thrust: booster-phase thrust and sustainer-phase thrust. The booster stage is used to accelerate the vehicle from zero velocity to a certain velocity, and then the sustainer stage is used to maintain a constant velocity. A typical thrust-time curve with all terminology for a DTRM is shown in figure 1. There are different methods to achieve this dual thrust profile such as two independent rocket motors, a single chamber with an intermediate nozzle, two separate grains with different geometries, different propellants.[1-3] In the case of two independent rocket motors, the booster motor is mechanically separated from the missile. For example, Russian air defence missiles SA-2 or SA-3 which give the benefit of reducing the final empty mass. However, this separation may have a negative impact on the environment and require some complex mechanism. In order to avoid separation problems, a dual-thrust motor composed of a single chamber is preferred. In this case, a grain with a certain design is required: the first phase with a large burning surface followed by a second phase with the smaller burning area. Some designs used the same grain configuration but with different propellant. In such a case, different thrust levels are achieved through a difference in burning rates as for example, M112 Motor in HAWK missiles [4] shown in figure 2. The most practical dual thrust motors use a single chamber with different grain geometries. For example, a radial burning grain for boost and end burning grain as sustain or radial star grain for boost and a tubular grain for sustain. As examples, tactical motors of Mk58 in AIM-7 Sparrow missile [5] shown in figure 3 or in Super-530 D air-to-air missile [6] shown in the figure 4, even though a few researchers are still using dual chamber rocket motor with the



cartridge loaded double base grains like the rocket motor for the booster for the Penguin MK2 MOD7 [7] missile shown in figure 5

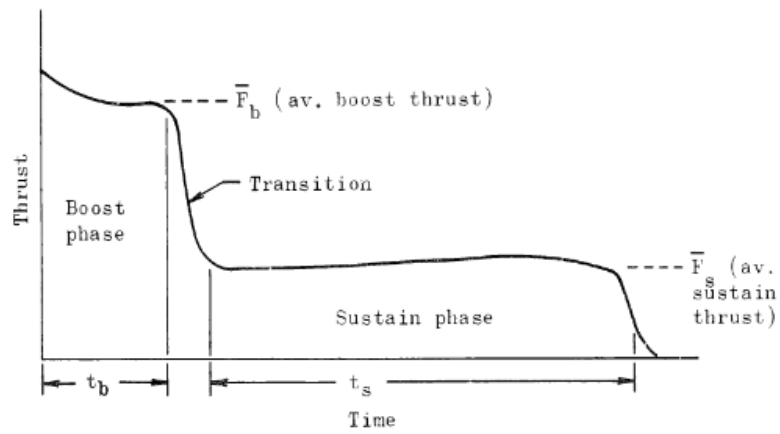


Figure 1. Boost- Sustain grain thrust-time curve [3].

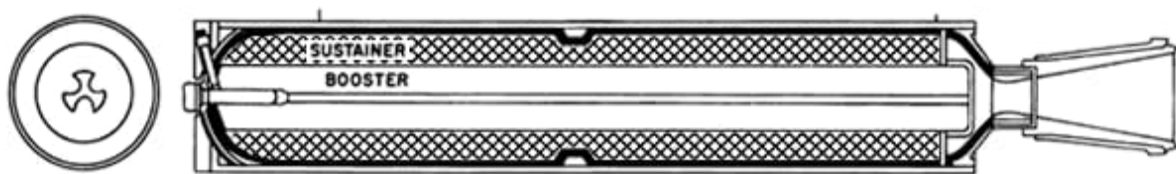


Figure 2. M-112 Hawk missile [4].

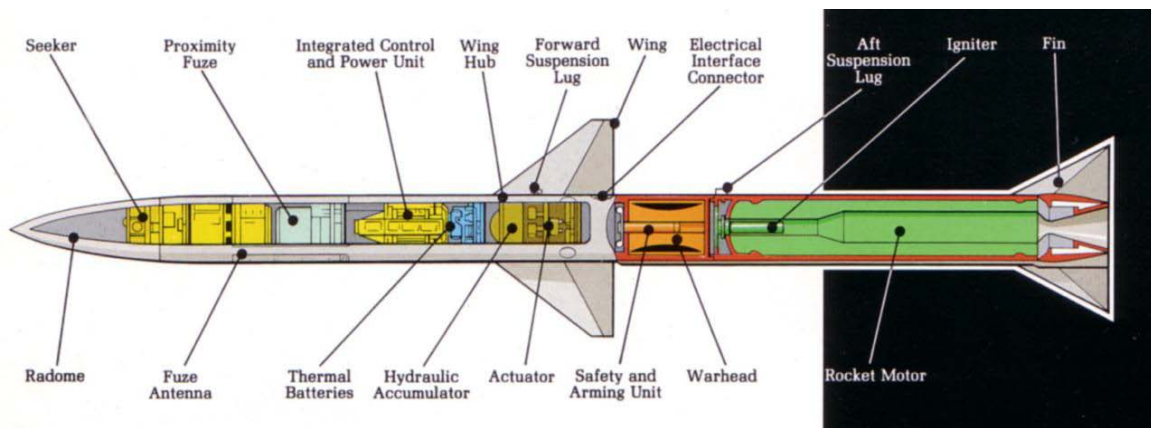


Figure 3. AIM-7 Sparrow missile [5].

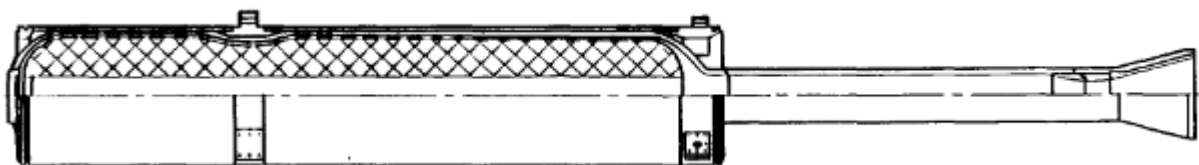


Figure 4. cross-section for super 530-D motor longitudinal [6].

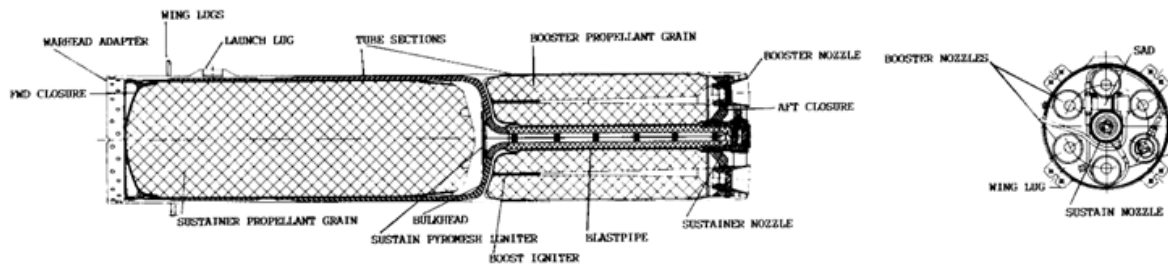


Figure 5. Penguin MK2-MOD7 rocket motor assembly [7].

Gawad [8] made two different methods to achieve DTRM'S, first by changing the burning area by single grain boost phase and second by changing the burning rate using dual end burning grain boost phase. He developed a mathematical model to estimate the pressure-time curve for DTRMs under geometric ballistic regression uncertainties, then made two experimental works: one for the 2-inch motor to get burning rate, and another for the 6-inch motor to get high thrust-to-weight ratio between booster and sustainer. This was made for two tubular grains with two different diameters along the grain. Ritchey and Anderson [9, 10] found that boost-sustain motors deliver specific impulse more effective than that delivered by boost ones, which makes the boost-sustain motors more suitable for certain applications.

Star grain, shown in figure 6, has been studied for more than 60 years. A previous survey showed that 40% of 129 operational motors used star grain [11] with number of star points ranging from 3-star points to the mighty 260 in SRM [12] the largest solid propellant ever built but did not fly, shown in figure 7. Grains with 16-star points [13] or 40-star points [14] shown in figures (8,9) respectively are used in the pyrogen for igniting the space shuttle solid booster separation motor. Star grain is characterized by several design parameters that provide good tailorability, in addition to higher volumetric loading than the traditional tubular grains.

The design variables of the star grain geometry are number of star points N , fillet radius f , angular fraction ϵ , star angle θ and maximum internal radius $(s + f)$. Typical values are $N = 7$, $f = 3$, $\epsilon = 0.5$, $\theta = 75^\circ$, $(s + f) = 60\text{mm}$. The star grain has two main phases of burning; the first phase can be designed to be progressive, regressive or neutral depending on the star angle (θ), and second phase which is always progressive.

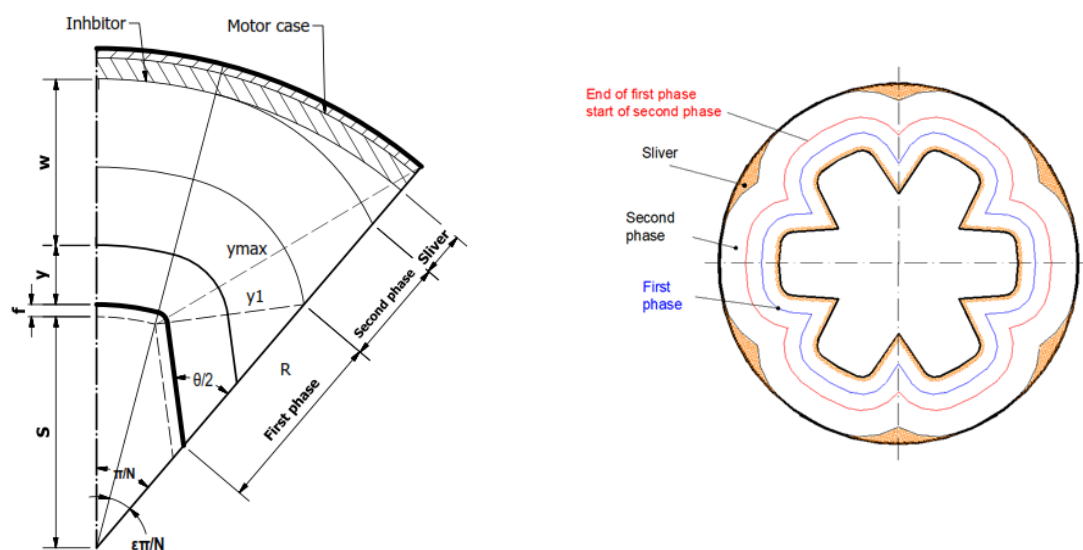


Figure 6. Star grain.

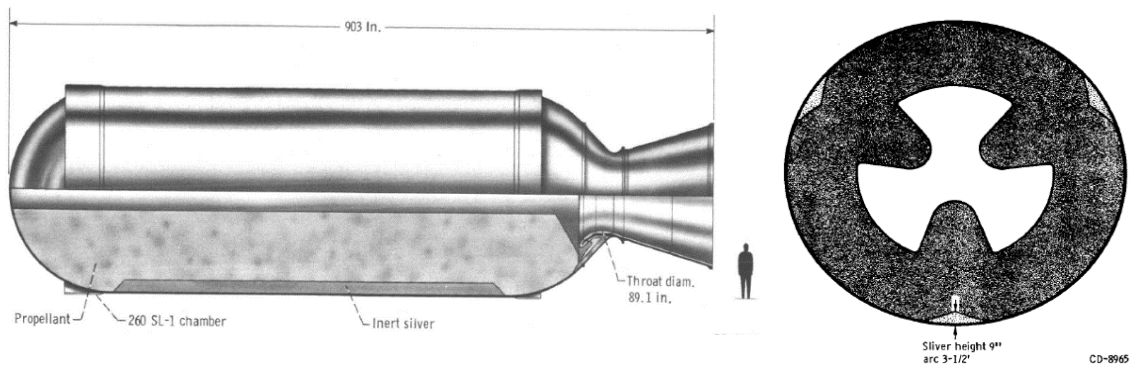


Figure 7. SRM with N=260 star points [12].

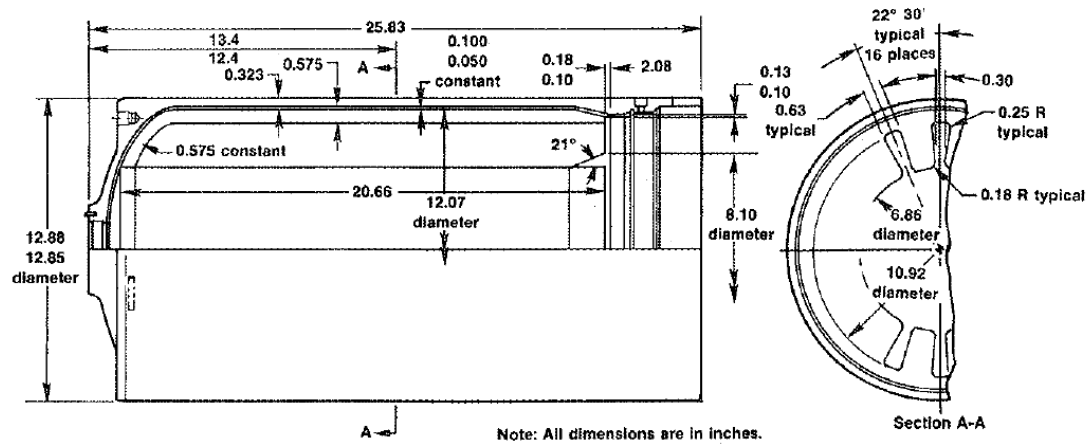


Figure 8. SRM with N=16 star points [13].

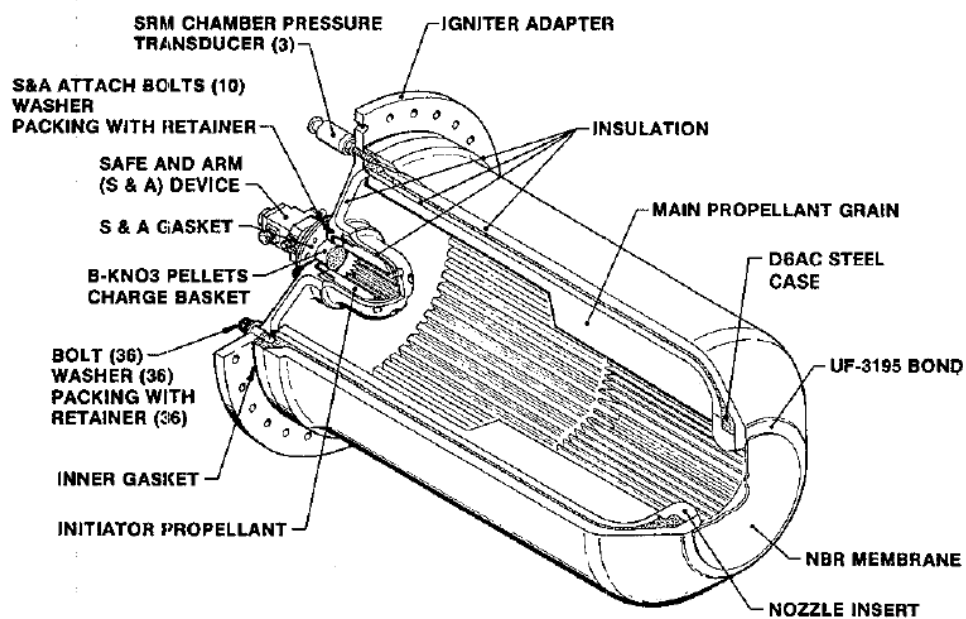


Figure 9. SRM with N=40 star points [14].

In 1992 Ricciardi [15] executed 16 conceivable configurations, 8 with convex and other 8 for concave points which have the boundaries $0 < r_2 < T_c$ and $(Y_t - \frac{T_c}{\sin \eta}) < r_2 < \sqrt{X_c^2 + Y_c^2}$ respectively as shown in figure 10. He described criteria and formulas adopted in developing a computer program capable of calculating the burning perimeter and evaluating the geometric evolution of a cylindrical star grain during its burning. If there is a variation of the seven geometrical parameters along the grain axis, the solutions have to be considered as approximated. If the cone semi angle is less than 10-15°, the error in area burning is less than 1-2% [15][15].

Stein [16] showed that star grain design increases volumetric loading efficiency (VLE) and specific impulse while keeping the pressure at a constant level in the combustion chamber. The idea of star grain design is to add more initial burn area that allows high starting up pressure and more neutral/regressive burn to achieve maximum efficiency.

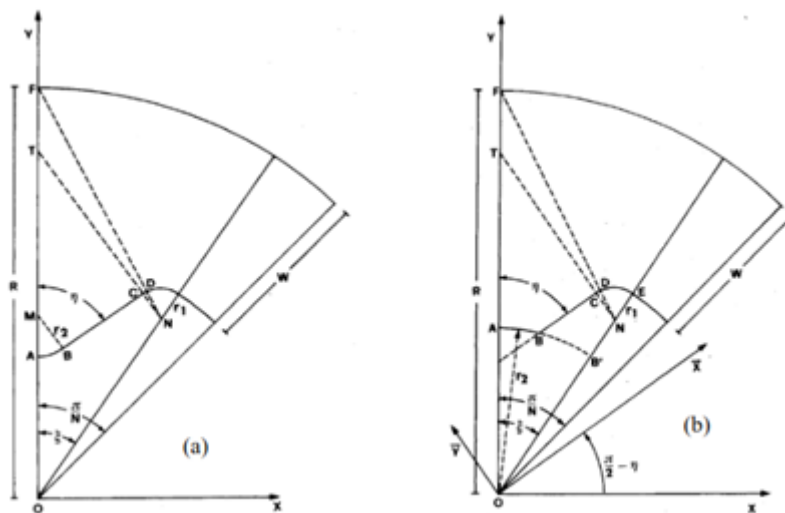


Figure 10. Star grain configuration for (a) convex and (b) concave [15].

Brooks[17] analysed and identified - for a given volumetric loading fraction - the most neutral-burning star with given web fraction, number of star points, and two small radii. He established a computer program that generates data for evaluating various other optimization criteria for star designs and to establish some universal limits of the capability of the star in terms of neutrality and sliver.

In this paper, a combination of two-star grains with different design parameters and different webs is used in order to achieve a dual thrust profile. The combination of design variables is calculated analytically followed by validation of the proposed design using a small-scale test motor. In addition, a genetic algorithm optimization module is used in order to tune the burning rate to fit the analytical data with experimental findings, and to predict the nozzle erosion rates as well.

2. Burn-back analysis of star grain

In all configurations studied, the grains have un-inhibited faces, thus the length of grain changes during burning. Two different types of transition geometries have been studied as shown in figure 11 where case (a) represents the sharp transition design and case (b) represents taper or conical transition design. The burn-back of the grains with sharp transition is shown in the figure 12 where the transition section is approximated using sharp edge to simplify the analytical equation rather than considering an arc of a circle with its center at the original transition plane. The case of taper transition is studied only experimentally and its analytical solution is beyond scope of this research.

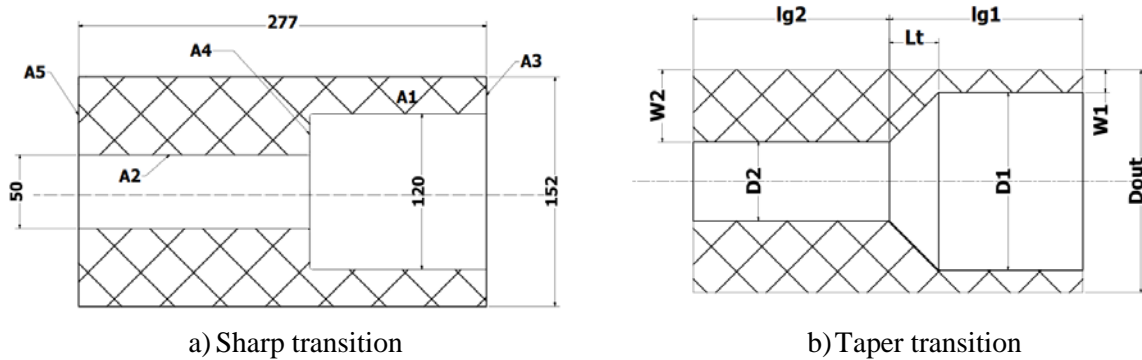


Figure 11. Longitudinal section for the different transition geometries.

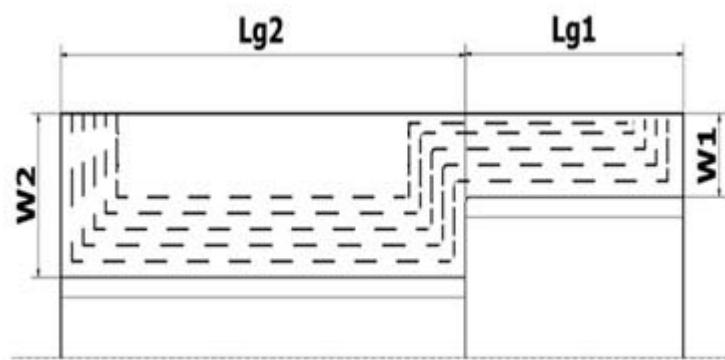


Figure 12. Burn-back of the grain with sharp transition.

In order to get neutral burning in the second phase, the grains will not have inhibited faces. Referring to Ricciardi [4], there are three types of configurations depending on web thickness (w), y_1 and y_{max} where y_1 is the condition of ending burning of the first phase as expressed in equation (1), and y_{max} is the maximum allowable burned distance of the propellant as in equation (2).

$$y_1 = s * \frac{\sin \frac{\epsilon \pi}{N}}{\cos \frac{\theta}{2}} - f \tag{1}$$

$$y_{max} = (R^2 + S^2 - 2RS \cos \frac{\epsilon \pi}{N})^{0.5} - f \tag{2}$$

Configurations 1, 2, and 3 correspond to ($y_1 < w$), ($w < y_1 < y_{max}$) and ($y_1 > y_{max}$) respectively. The details of these configurations are given below.

2.1. Configuration 1: ($y_1 < w$), figure 13

This configuration is divided into three zones: zone 1: ($0 \leq y \leq y_1$), zone 2 ($y_1 < y \leq w$) and zone 3 ($w < y \leq y_{max}$).

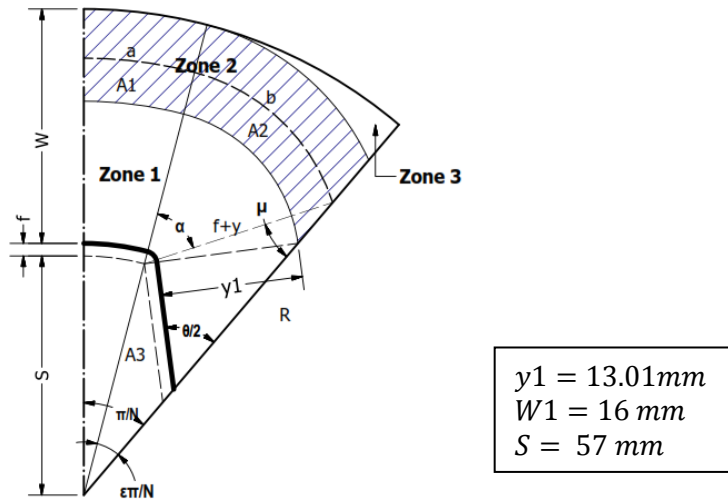


Figure 13. The geometry of configuration 1.

Zone 1: (0 ≤ y ≤ y₁)

The burning area (A_b) of the surface as a function of burnt distance y is calculated by equation (3):

$$A_b = 2Nl_g(a + b + c) = 2Nl_g[(s + f + y) \left(\frac{\pi}{N} - \epsilon \frac{\pi}{N}\right) + (f + y) \left(\frac{\pi}{2} + \epsilon \frac{\pi}{N} - \frac{\theta}{2}\right) + s \frac{\sin \epsilon \frac{\pi}{N}}{\sin \frac{\theta}{2}} - (f + y) \cot \frac{\theta}{2}] \quad (3)$$

The corresponding port area (A_p) of gases is found using equation (4):

$$A_p = 2N(A_1 + A_2 + A_3 + A_4 + A_5) = N \left[(s + f + y)^2 \left(\frac{\pi}{N} - \epsilon \frac{\pi}{N}\right) + (f + y)^2 \left(\frac{\pi}{N} + \epsilon \frac{\pi}{N} - \frac{\theta}{2}\right) + (f + y)^2 \cot \frac{\theta}{2} + s^2 \frac{\sin \epsilon \frac{\pi}{N}}{\sin \frac{\theta}{2}} \sin \left(\frac{\theta}{2} - \epsilon \frac{\pi}{N}\right) + (f + y) \left(s \frac{\sin \epsilon \frac{\pi}{N}}{\sin \frac{\theta}{2}} - (f + y) \cot \frac{\theta}{2}\right) \right] \quad (4)$$

Zone 2: (y₁ < y ≤ w)

The burning area of the surface in zone 2 as the surface progresses a distance y is calculated by equation (5):

$$A_b = 2Nl_g \left[(s + f + y) \left(\frac{\pi}{N} - \epsilon \frac{\pi}{N}\right) + (y + f) \left[\epsilon \frac{\pi}{N} + \sin^{-1} \left(\frac{s}{y+f} \sin \epsilon \frac{\pi}{N} \right) \right] \right] \quad (5)$$

The port area is found using equation (6):

$$A_p = N \left[(s + f + y)^2 \left(\frac{\pi}{N} - \epsilon \frac{\pi}{N}\right) + (f + y)^2 \left[\epsilon \frac{\pi}{N} + \sin^{-1} \left(\frac{s}{y+f} \sin \epsilon \frac{\pi}{N} \right) \right] + s(f + y) \sin \left[\pi - \epsilon \frac{\pi}{N} - \sin^{-1} \left(\frac{s}{y+f} \sin \epsilon \frac{\pi}{N} \right) \right] \right] \quad (6)$$

Zone 3: (Sliver Area) (w < y ≤ y_{max})

In this zone, both segment b and segment c vanish, thus the burning area of the surface in zone 3 as the surface progresses a distance y is calculated using equation (7):

$$A_b = 2Nl_g(f + y)(\phi - \delta) \quad (7)$$

where $\delta = 180 - \cos^{-1} \left[\frac{s^2 + (f+y)^2 - R_{out}^2}{2s*(f+y)} \right]$

The port area can be expressed as in equation (8)

$$A_p = N \left[R_{out}^2 \left(\frac{\pi}{N} - \frac{\varepsilon\pi}{N} \right) + s(f+y)\sin \left(\mu + \frac{\varepsilon\pi}{N} \right) + 0.5\beta R^2 - 0.5Rs * \sin \beta + (f+y)^2\Gamma \right] \quad (8)$$

where $\beta = \cos^{-1} \frac{R^2+s^2-(f+y)^2}{2Rs}$

2.2. Configuration 2: ($w < y_1 < y_{max}$), figure 14

Configuration 2 is divided into three zones, 1, 3 and 4. Zone 1 ($0 \leq y \leq w$) is the same as zone 1 in configuration 1, and zone 3 ($y_1 < y \leq y_{max}$) is the same as zone 3 in configuration 1. So, zone 4 is the new zone in this configuration.

Zone 4: ($w < y \leq y_1$)

The burning area of the surface in zone 4 as the surface progresses a distance y is expressed by equation (9):

$$A_b = 2NL_g(a+c) = 2NL_g \left[(f+y) * (\alpha - \delta) + \frac{y_1-y}{\tan \frac{\theta}{2}} \right] \quad (9)$$

Port area can be calculated using equation (10):

$$A_p = 2N * (A_1+A_2+A_3+A_4)$$

$$A_p = N \left[R^2 \left(\frac{\pi}{N} - \frac{\varepsilon\pi}{N} \right) + R^2\phi - Rs \sin \phi + (f+y)^2\Gamma \right. \\ \left. + s(f+y) \cos \left(\frac{\theta}{2} - \frac{\varepsilon\pi}{N} \right) - C(y_1 - y) \right] \quad (10)$$

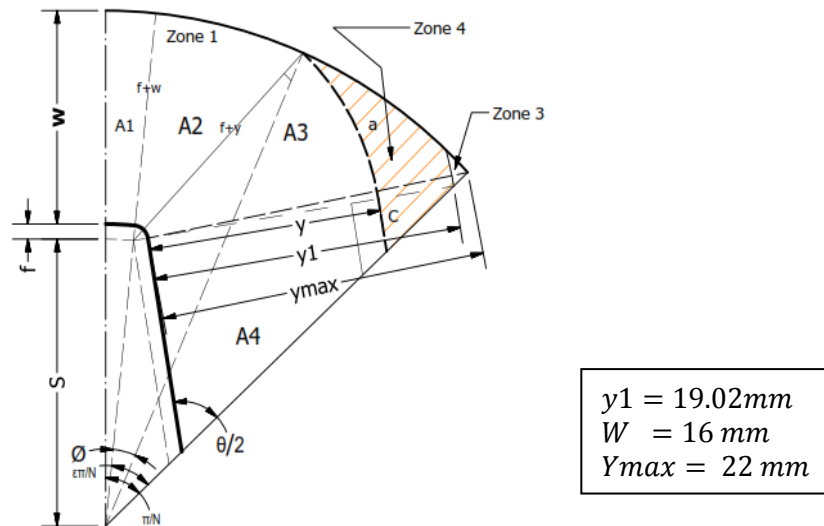


Figure 14. The geometry of configuration 2.

2.3. Configuration 3: ($y_1 > y_{max}$), figure 15.

This configuration can be divided into three zones: Zone 1 ($0 < y \leq w$) is the same as zone 1 in configuration 1, and zone 4 ($w < y \leq CQ_0$) is the same as zone 4 in configuration 2.

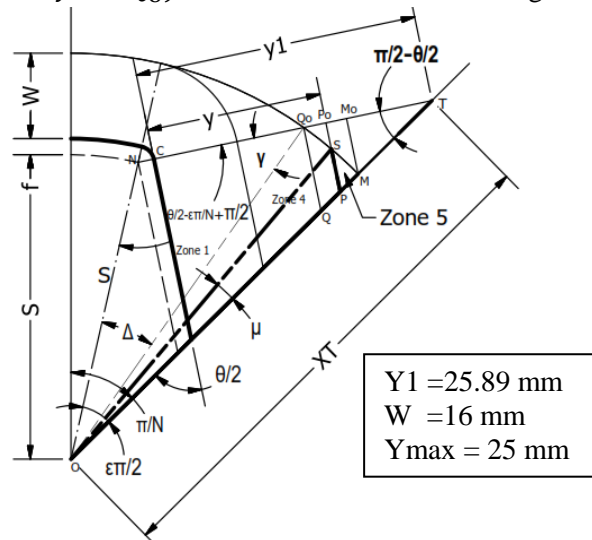


Figure 15. The geometry of configuration 3.

Zone 5: ($CQ_0 < y < CM_0$)

The burning area of the surface in zone 5 as the surface progresses a distance y is calculated using equation (11):

$$A_b = 2Nl_g \left[X_p \cos \frac{\theta}{2} + \sqrt{R^2 - X_p^2 \left(\sin \frac{\theta}{2} \right)^2} \right] \tag{11}$$

Port area is calculated by using equation (12)

$$A_p = N \left[\left(R^2 \left(\frac{\pi}{N} - \mu \right) + R * \overline{O_p} * \sin \mu \right) \right] \tag{12}$$

where

$$X_p = X_T - \frac{y_1 - y_C}{\sin \frac{\theta}{2}}$$

$$X_T = S \left(\cos \varepsilon \frac{\pi}{N} + \sin \varepsilon \frac{\pi}{N} \tan \frac{\theta}{2} \right)$$

$$\overline{O_p} = \frac{R * \sin \left(\frac{\theta}{2} - \mu \right)}{\sin \frac{\theta}{2}}$$

The governing expressions for burning area in each phase are summarized in the following table 1. These areas are: AB1= the surface burning area of star 1., AB2 = the surface burning area of star 2, AB3 = the first surface burning area related to star 1, AB4 = the middle surface burning area between star 1, 2, and finally AB5 = the last surface burning area related to star 2. The resulting total burning area is shown in figure16 with individual burning areas for different surfaces. However, a long transition between booster and sustainer is observed. In addition, the booster time is too long, and the sustainer time is short. The desired objective is not achieved and hence SRM is to be modified to improve the results. After several trials, an acceptable solution for the transition between booster and sustainer, and the relative times of booster and sustainer have been reached. Design parameters for the accepted dual thrust profile are shown in figure 17.

Table 1. Summary for burning surfaces and how to calculate (refer to figure 1(a) for surface numbering).

	$Y = 0$	$Y_2 = 3.200$	$Y_1 = 13$	$W_1 = 16$	$Y_{max1} = 21$	$W_2 = 51$	$Y_{max2} = 51.80$
AB1	Zone1 ($Y > 0 \ \& \ Y < Y_1$)	Zone2 ($Y > Y_1 \ \& \ Y \leq W_1$)	Zone3 ($Y > W_1 \ \& \ Y \leq Y_{max1}$)	Zero	AB1	Zone1 ($Y > 0 \ \& \ Y < Y_1$)	Zone2 ($Y > Y_1 \ \& \ Y \leq W_1$)
AB2	First phase $Y \leq Y_2$	Second phase $Y \leq W_2 \ \& \ Y > Y_2$	Sliver phase $Y > W_2 \ \& \ Y \leq Y_{max2}$		AB2	First phase $Y \leq Y_2$	Second phase $Y \leq W_2 \ \& \ Y > Y_2$
AB3	$A_{C,CH} - A_{P1}$	$A_{C,CH} - A_{P1}$	$A_{C,CH} - A_{P1}$	$A_{C,CH} - A_{P1}$		Zero	
AB4	$A_{P1} - A_{P2}$	$A_{P1} - A_{P2}$	$A_{P1} - A_{P2}$	$A_{P1} - A_{P2}$	$A_{P1} - A_{P2}$	$A_{P1} - A_{P2}$	$A_{P1} - A_{P2}$
AB5	$A_{C,CH} - A_{P2}$	$A_{C,CH} - A_{P2}$	$A_{C,CH} - A_{P2}$	$A_{C,CH} - A_{P2}$	$A_{C,CH} - A_{P2}$	$A_{C,CH} - A_{P2}$	$A_{C,CH} - A_{P2}$

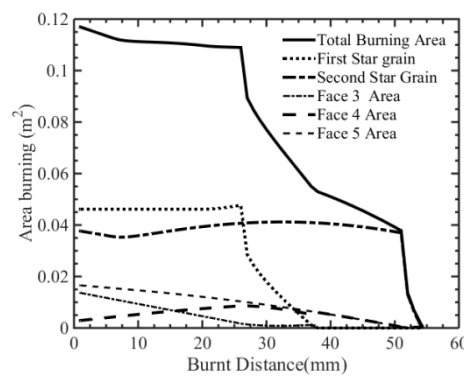


Figure 16. Calculated burning area for all surfaces, $N=5$, $\epsilon=0.8$, $f=5\text{mm}$, $w_1=26\text{ mm}$, $w_2=51\text{ mm}$, $lg_1=97\text{ mm}$, $lg_2=180\text{ mm}$, $s_1=45\text{mm}$, $s_2=20\text{mm}$, $D_1=100\text{ mm}$, $D_2=50\text{ mm}$ and θ (Neutral) $=62.24^\circ$.

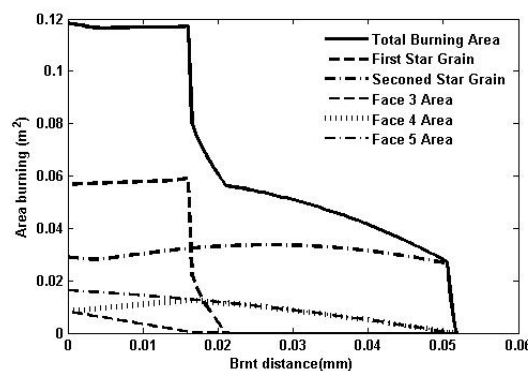


Figure 17. Calculated burning area for all surfaces, $N=7$, $\epsilon=0.5$, $f=3\text{mm}$, $w_1=16\text{ mm}$, $w_2=51\text{ mm}$, $lg_1=120\text{ mm}$, $lg_2=157\text{ mm}$, $s_1=57\text{mm}$, $s_2=22\text{mm}$, $D_1=120\text{ mm}$, $D_2=50\text{ mm}$ and $\theta =75^\circ$.

The flowchart of burn-back analysis for each configuration to get the area burning module $A_B(Y)$ is shown in figure 18 consequently.

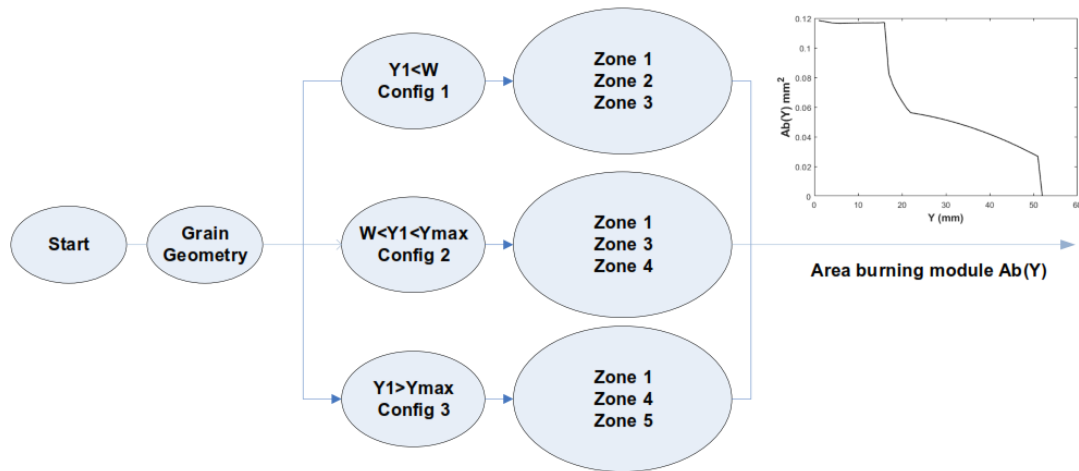


Figure 18. Flowchart of grain burn-back analysis.

3. Internal ballistics

In order to predict the pressure-time curve, the values of burning rate from composite propellant were obtained from the experiments using 2” motor of [8] which gave the preliminary data of the value for pressure exponent ($n=0.021$) and burning rate coefficient ($a=2.68 \times 10^{-4}$) for the proposed design, a 0-D internal ballistic prediction module (IBPM) was applied. The basic equation for this module according to [2] is:

$$V_c \frac{dP_c}{dt} = \rho_{sp} R T_c A_b a P_c^n - \Gamma P_c A_{cr} \sqrt{R T_c} \tag{13}$$

where V_c = chamber free volume, P_c = combustion pressure (stagnation pressure), ρ_{sp} = solid propellant density, R = gas constant, T_c = combustion temperature, A_b = burning area, and A_{cr} = nozzle critical area, according to the flowchart of input and output data for IBPM as shown in figure 19. In order to predict the pressure-time curve, the solution of equation 13 was performed according to the flow chart shown in figure 20. The resultant pressure time curve is shown in figure 21.

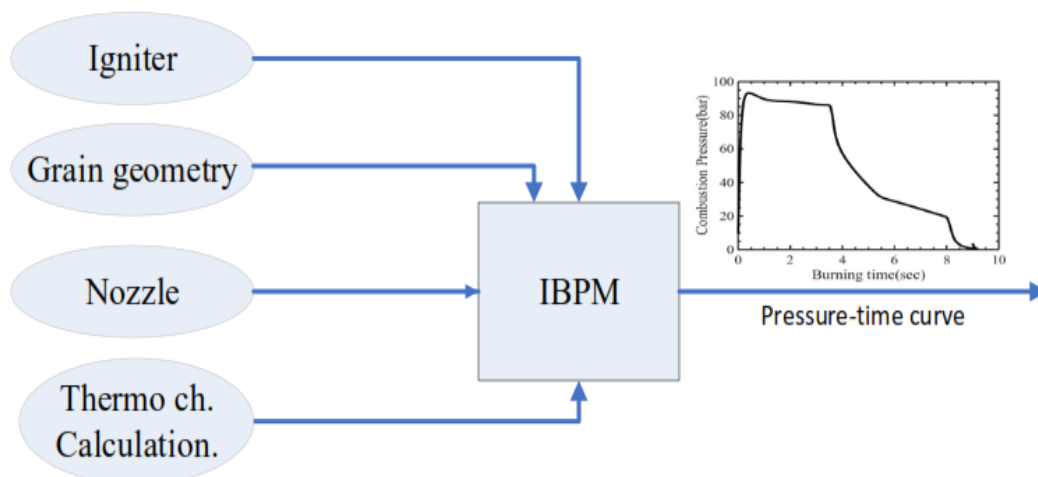


Figure 19 Flowchart of input and output data of IBPM.

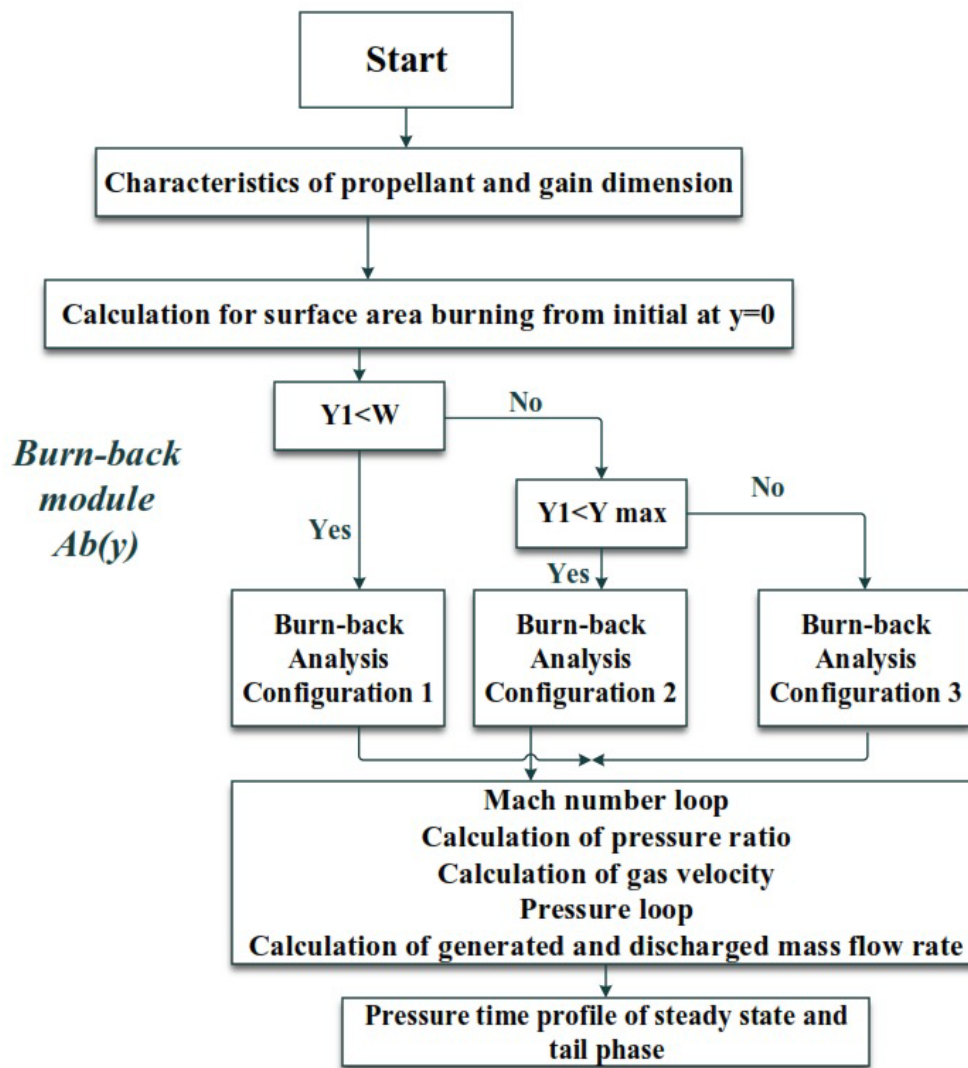


Figure 20. Flow chart of IBPM.

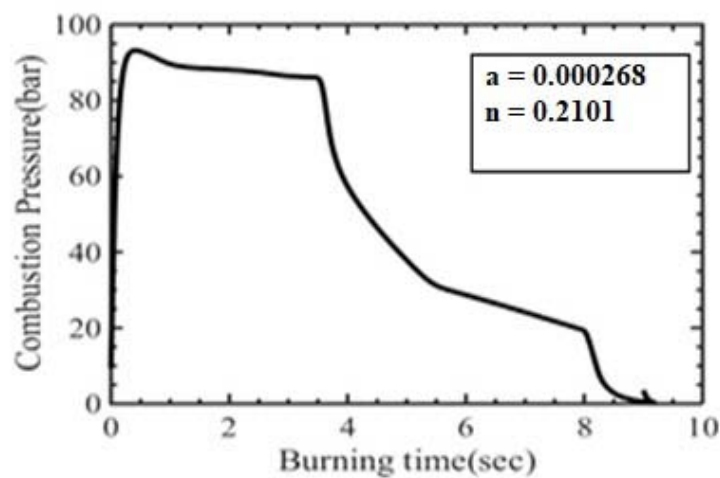


Figure 21. Predicted pressure-time curve for the proposal grain.

4. Experimental results and discussions

In order to validate the burn-back analysis of the proposed grain and the 0-D internal ballistic module, a small-scale test motor (6" motor) was used, figure 22. In order to study the effect of transition geometry on thrust time-curve, two mandrels were used in propellant casting in a small-scale test motor shown in the figure 23 with the geometry of resultant grains demonstrated in figures 24 and 25. The experimental results of sharp and taper geometry from factory 18 are shown in table 2. In order to obtain different operating pressures, different nozzles with different throat diameters were used. Table 3 shows test matrix.

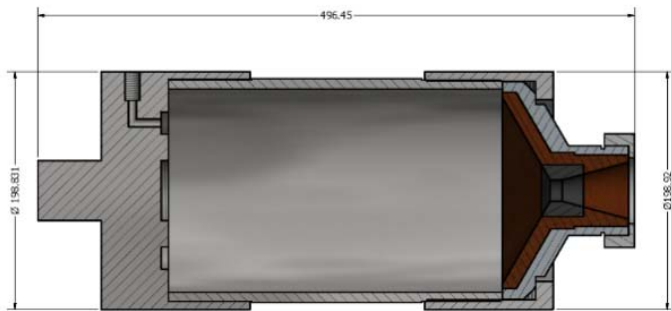


Figure 22. Small scale test motor used in experiments.



Figure 23. Taper and sharp mandrels used in SPRM.

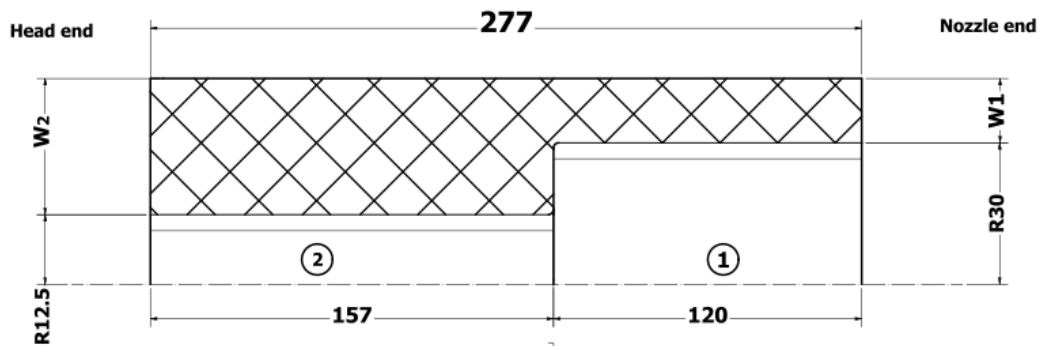


Figure 24. Main dimensions of sharp star grain.

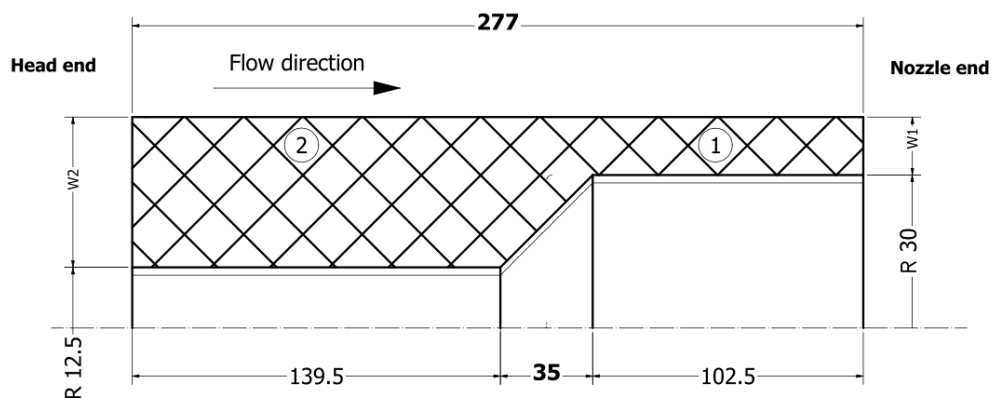


Figure 25. Main dimensions of taper star grain.

Table 2. Results for sharp and taper geometries.

Geometry	Temp (C)	Throat D_{cr} (mm)	m_p (kg)	T50% (Sec)	Pmax (BAR)	P50% (BAR)	R50% (mm/s)	C* (m/s)	Isp sec
Sharp	20	15	6.4	4.982	156.3	97.44	8.58	1357	229.5
	20	18	6.4	6.365	96.2	56.26	6.72	1460	220.0
Taper	21	15	6.9	5.940	140.8	80.33	8.59	1395	229.5
	21	18	6.9	7.000	91.9	50.57	7.29	1476	221.3

Table 3. Experimental test matrix.

	Sharp	Tapered
$\phi 15$	A1	B1
$\phi 18$	A2	B2

The following figures. (26-29) illustrates the effect of using different transition geometries on pressure-time and thrust-time traces in case of throat diameters 15 and 18 mm respectively.

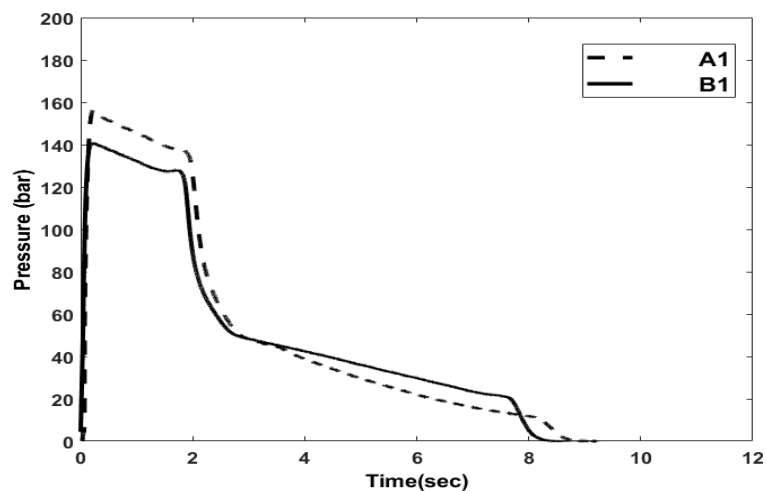


Figure 26. Pressure time curves for different transition geometries at the same throat.

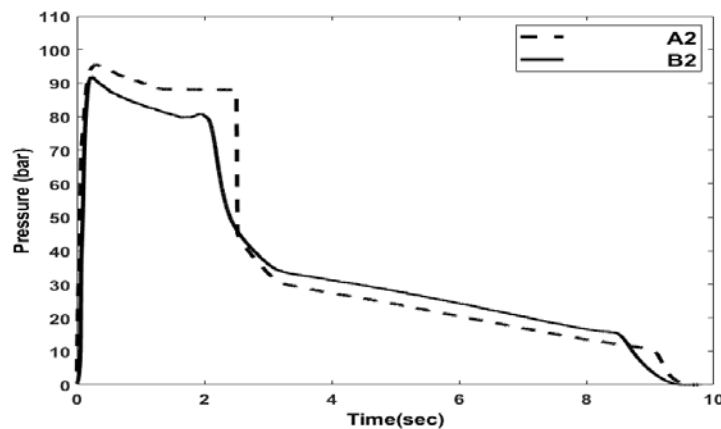


Figure 27. Pressure time curves for different transition geometry at the same throat.

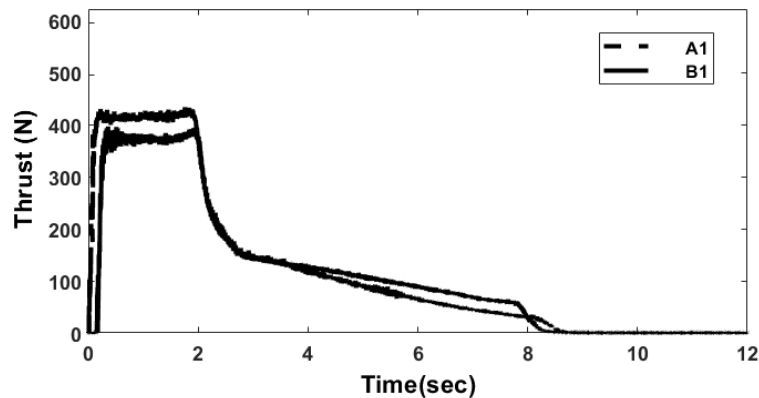


Figure 28. Thrust time curves for different transition geometry at 18 mm.

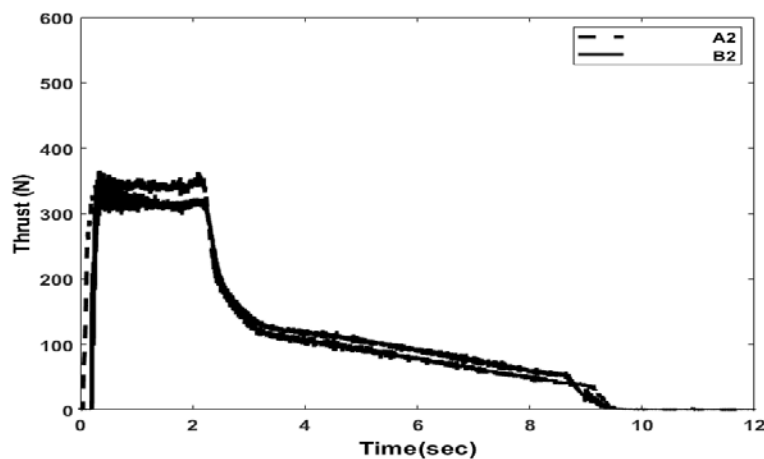


Figure 29. Thrust time curves for different transition geometry at 15mm.

From the previous figures, Basically, there is no difference in performance between taper transition and sharp transition. The tapered transition gives lower pressure in the booster phase due to lower initial burning surface. In addition, the taper configuration gives a clear advantage of higher volumetric loading, as the motor with the same size carries 6.9 kg in comparison to 6.4 kg for a case of sharp configuration.

5. Optimization module

In order to decrease the difference between the measured and predicted pressure-time curves and the predicted optimization module, genetic algorithm module in MATLAB, was used as illustrated by the flowchart in figure 30.

After many trials, the minimum error is reached with assuming different burning rates; one at lower pressure and one at higher pressure. As evident from [18], the composite propellant with bimodal ammonium perchlorate has a region of plateau burning with different burning rates before and after plateau region. The fitted pressure-time curve is shown in figure 31. The results of optimization for case A1 are as follows: $n_h=0.2247$, $a_h=2.1727 \times 10^{-4}$, $n_1=0.213$, $a_1=2.342 \times 10^{-4}$, $P=62.19$ bar. A summary for propellant data before and after tuning using optimization module is shown in table 4. Comparing pressure-time curves which shows a progressive profile in the boost phase while the corresponding thrust-time curves show neutral profile, giving evidence of nozzle erosion. This erosion is validated by inspecting images of the nozzle throat after motors burnout as shown in table 5.

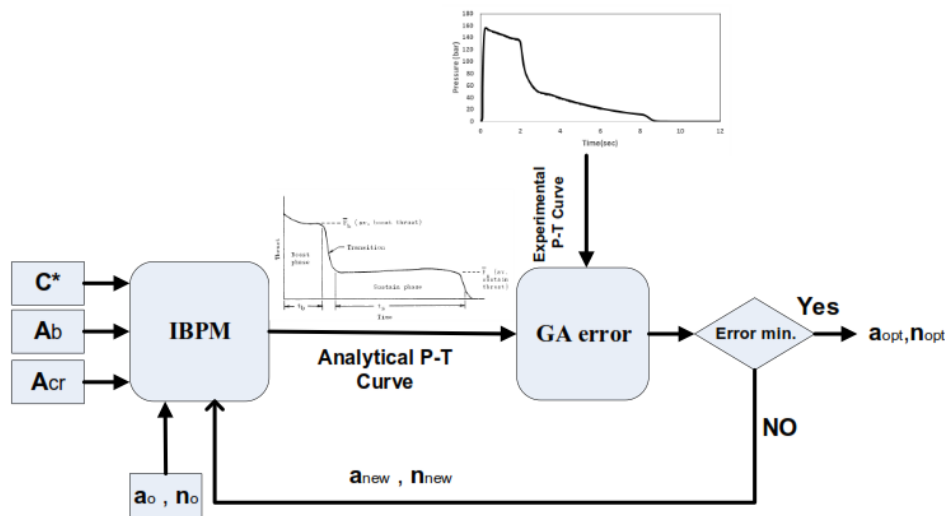


Figure 30. Flowchart of optimization module.

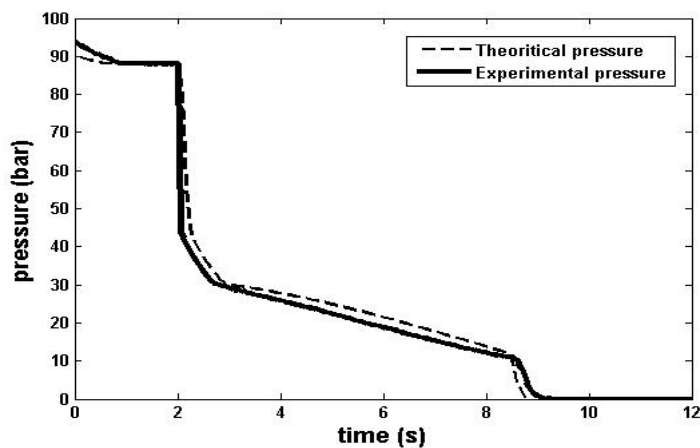


Figure 31. Pressure time curves for experimental and theoretical work at throat 18 mm.

Table 4. Experimental test matrix.

	Before tuning	After tuning	
		Low pressure region	High pressure region
a	2.68×10^{-4}	2.342×10^{-4}	2.1727×10^{-4}
n	0.213	0.213	0.2247

In addition to tuning the burning rate law parameters, an additional parameter- nozzle erosion rate- is included in the optimization module. A summary for the predicted and experimental erosion rates is shown in table 6. The comparison between nozzle erosion rates for different initial throat diameter shows that erosion rate for smaller throat diameter which gives a higher combustion pressure yield a larger erosion rate than that of initially large throat diameter. Such result is in agreement with previous researches [19]. From table 6, there is a good agreement between measured and predicted erosion rates. However, the result for case A2 shows a larger discrepancy between the measured average erosion rate and the erosion rate calculated from optimization module.

Table 5. Nozzles before and after static firing.

Cases	A1(ϕ 15)	A2(ϕ 18)
Before firing		
After firing		
Graphite insert		

Table 6. Erosion rate from optimization module.

Case	A1	A2
D_{Cro} After burning	ϕ 15.6	ϕ 18.3
Average erosion rate (mm/s)	0.0375	0.01875
Predicted erosion rate (mm/s)	0.03358	0.0125

6. Conclusion

Star grain showed a good tailorability. As with only changes of star grain design parameters, there is good controllability on both relative durations of booster and sustainer phase, and, the transition between the booster phase and the sustainer phase. This tailorability comes at the cost of more complicated analytical burn-back where different configurations with each configuration have multi-zone with different burning regimes. Different transition (i.e. sharp transition vs. taper transition) were compared, with tapered transition is shown to give a comparable performance with the sharp transition with the advantage of higher volumetric loading.

The analytical procedure for predicting the pressure-time trace for a dual thrust rocket motor (0-D internal ballistic module) is derived and validated for sharp transition geometry at different throat diameter 0-D internal ballistic module showed to give very good fit to experimental data as long as the burning rate law is accurate, but in case of uncertainty in burning rate law, A GA-Module can be applied to find the more accurate data. In addition, combining the 0-D internal ballistic module with GA-module can be used to predict the erosion rates in a nozzle with a good fit with the experimental data, with higher combustion pressure leads to higher nozzle erosion rates as known from previous analytical and experimental researches.

References

- [1] Barrere M, Jaumotte A, Fraeijs de Veubeke B and Vandekerckhove J V 1960 *Rocket propulsion* (Liège: Belgium LTAS)
- [2] Sutton G P and Ross D M 1976 *Rocket propulsion elements : An Introduction to the engineering of rockets* (John Wiley & Sons 4th ed)
- [3] Bornstein L J 1979 Method of making dual-thrust rocket motor *Google Patent*.
- [4] *Operator, organizational, direct and general support maintenance manual : intercept-aerial guided missile MIM-23B, MTM-23B, and M18E2 : improved HAWK air-defense guided missile system 1984* (Washington, D.C. Headquarters Dept. of the Army).
- [5] Kopp C BAe Active Skyflash and AIM-120 AMRAAM 1994 *Australian Aviation June 1994*.
- [6] TRICOT J 1988 Wrap-on composite case technology Super 530 D-Tactical motor application 24th *Joint Propulsion Conference* p 3326.
- [7] Haugen S 1990 Development and pre-qualification of the booster rocket motor for the Penguin MK2 MOD7 missile 26th *Joint Propulsion Conference* p.1863.
- [8] Abdel Gawad A R, Mohamed MY, Abdalla H M, and Elsenbawi M A 2015 Analytical Prediction of Dual-Thrust Rocket motors under Uncertainties *International Conference on Aerospace Sciences and Aviation Technology* pp 1-12.
- [9] Ritchey H 1955 Tailor-Made Thrust *Jet Propulsion* **25** p55.
- [10] Anderson S 1964 Design and Evaluation of a Propulsion Unit for a Single-Stage Hercules (U) *Rep. S-48, Redstone Arsenal Research Div., Rohm and Haas Co.(Huntsville, AL) July 8*.
- [11] Brooks W 1972 *Solid propellant grain design and internal ballistics* vol. 8076(WashingtonD.C National Aeronautics and Space Administration).
- [12] Crimmins P, Cousineau M, Rogers C, and Shell V 1999 The 260-The largest solid rocket motor ever tested 36th *AIAA/ASME/SAE/ASEE Joint Propulsion Conference and Exhibit* p. 3690.
- [13] SMITH G and CHASE C 1976 Space shuttle booster separation motor design 12th *Propulsion Conference* p 772.
- [14] Adams I and Call F 1979 *Space shuttle SRM development* (NASA Technical Reports).
- [15] Ricciardi A 1992 Generalized geometric analysis of right circular cylindrical star perforated and tapered grains *Journal of Propulsion and Power* **8** pp. 51-58.
- [16] Stein S. D. 2008 Benefits of the Star grain Configuration for a Sounding Rocket(United States: Air Force Academy Department of Astronautics, USAFA).
- [17] Brooks W T 1982 Ballistic optimization of the star grain configuration," *Journal of spacecraft and rockets* **19** pp 54-59.
- [18] Ghazimirsaid M S A, Audet A and Koch C R 2008 HCCI Engine Cyclic variation characterization using both chaotic and statistical approach *Proceedings of Combustion Institute-Canadian Section*, University of Toronto, Ontario.

Acknowledgments

The authors would like to thank the experts in the Abo-Zaabal factory and test facility for their generous support and valuable contribution.